PCCP

ROYAL SOCIETY OF CHEMISTRY

PAPER

View Article Online
View Journal | View Issue

Check for updates

Cite this: *Phys. Chem. Chem. Phys.*, 2021, **23**, 2438

Tracer diffusion coefficients of Li^+ ions in *c*-axis oriented Li_xCoO_2 thin films measured by secondary ion mass spectrometry

Gen Hasegawa,[ab] Naoaki Kuwata, *[ab] Yoshinori Tanaka,[a] Takamichi Miyazaki,[c] Norikazu Ishigaki,†[b] Kazunori Takada [a] and Junichi Kawamura ‡[b]

Lithium diffusion is a key factor in determining the charge/discharge rate of Li-ion batteries. Herein, we study the tracer diffusion coefficient (D^*) of lithium ions in the *c*-axis oriented $LiCoO_2$ thin film using secondary ion mass spectrometry (SIMS). We applied a step-isotope-exchange method to determine D^* in the Li-extracted Li_xCoO_2. The observed values of D^* ranged from 2×10^{-12} to 3×10^{-17} $cm^2\ s^{-1}$ depending on the compositions in the range of $0.4 < x < 1.0$. Approaching the stoichiometric composition ($x = 1.0$), D^* decreases steeply to the minimum, which can be explained by the vacancy diffusion mechanism. Electrochemically determined diffusion coefficients corrected by thermodynamic factors are found to be in good agreement with D^* determined by our method, over a wide range of compositions. The *c*-axis diffusion was explained by the migration of Li^+ ions from one layer to another through additional diffusion channels, such as antiphase boundaries and a pair of Li antisite and oxygen vacancies in cobalt oxide layers.

Received 31st August 2020,
Accepted 17th December 2020

DOI: 10.1039/d0cp04598e

rsc.li/pccp

Introduction

The knowledge of the diffusion behaviour of Li^+ ions in Li-insertion electrodes is essential for understanding the charge–discharge mechanism of the electrodes, which enables us to improve the performance of Li-ion batteries (LIBs). The layered structure of $LiCoO_2$ (LCO), the best-known cathode material for LIBs, exhibits high rate capability and excellent cycle stability.[5,6] LCO has shown excellent performance in solid-state batteries,[7–9] making it attractive for a wide range of applications, including microelectronics and electric vehicles.[10,11]

LCO has a two-dimensional diffusion path parallel to the *ab*-plane. The vacancy diffusion mechanism has been predicted by the density functional theory (DFT) calculations, and formation of divacancies has been found to reduce the activation energy (E_a) of Li^+ ion migration.[12–14] The calculations show that the diffusion coefficient in the *ab*-plane of $Li_{0.6}CoO_2$ is about 10^{-9} $cm^2\ s^{-1}$,[12,13] although there is some uncertainty in the absolute value. In the ideal LCO structure, there is no diffusion path in the *c*-axis direction. However, experimentally, Li ions can be extracted and inserted along the *c*-axis direction,[9,15] which has been confirmed in the all-solid-state batteries based on *c*-axis oriented thin films[4,7–9] and epitaxial thin films.[16] Grain boundaries as a pathway for Li diffusion has been proposed by DFT calculations.[17,18] Nanoscale atomic force microscopy also suggests fast Li diffusion near the grain boundaries.[19–21] However, no direct measurement of the diffusion coefficient of lithium ions along the *c*-axis of $LiCoO_2$ has been reported.

Diffusion coefficients of LCO have been reported so far by many authors, which were measured by electrochemical techniques as the chemical diffusion coefficients ($\tilde{D}$). Table 1 summarizes the reported values of $\tilde{D}$ of LCO. The values of $\tilde{D}$ reported in the literature vary from 10^{-13} to 10^{-8} $cm^2\ s^{-1}$ for powders and 10^{-14} to 10^{-9} $cm^2\ s^{-1}$ for thin films. The large discrepancies are attributed to the intrinsic uncertainty involved in the experiments.[22] The electrochemical system involves multiple bulk and interfacial processes (*e.g.*, ohmic resistances in the electrolyte, interfacial charge transfer resistance and side reactions[23–26]), which often make the analysis difficult. In addition, self-diffusion coefficients were measured by NMR and muon-spin relaxation techniques.[27,28] These techniques estimate the jump rate of Li^+ ions from the relaxation phenomena.

---

[a] *National Institute for Materials Science (NIMS), 1-1 Namiki, Tsukuba 305-0044, Japan. E-mail: KUWATA.Naoaki@nims.go.jp*
[b] *Institute of Multidisciplinary Research for Advanced Materials, Tohoku University, 2-1-1 Katahira, Aobaku, Sendai 980-8577, Japan*
[c] *School of Engineering, Tohoku University, 6-6-11 Aramaki-aza Aoba, Aoba-ku, Sendai, 980-8579, Japan*

† Present address: National Institute of Advanced Industrial Science and Technology (AIST), 1-1-1 Higashi, Tsukuba 305-8565, Japan.

‡ Present address: University Research Administration (URA) Center, Office of Research Promotion, Tohoku University, 2-1-1 Katahira, Aobaku, Sendai 980-8577, Japan.

Table 1 Literature review of chemical diffusion coefficients for the Li_xCoO_2 powder and thin film electrodes. The thin films were prepared by electrostatic spray deposition (ESD), pulsed laser deposition (PLD), and radio frequency magnetron sputtering (RF sp.). The electrochemical techniques used include the potentiostatic intermittent titration technique (PITT), the galvanostatic intermittent titration technique (GITT), and electrochemical impedance spectroscopy (EIS)

Sample	Technique	$\tilde{D}$ ($cm^2\ s^{-1}$)	Li composition (potential)	Ref.
Powder	PITT	5×10^{-9}	$0.2 < x < 0.8$	Mizushima[5]
Powder	GITT, PITT	2×10^{-9}–4×10^{-8}	$0.10 < x < 1$	Honders[39]
Powder	EIS	5×10^{-8}	$x = 0.65$	Thomas[40]
Powder	GITT	4×10^{-9}–1×10^{-8}	$0.5 < x < 0.75$	Choi[41]
Powder	PITT	1×10^{-10}–2×10^{-9}	$0.35 < x < 0.85$	Barker[42]
Powder	PITT	5×10^{-12}–1×10^{-10}	3.8–4.4 V	Aurbach[43,44]
Powder	PITT	10^{-13}–10^{-12}	$0.5 < x < 0.95$	Okubo[45]
Single particle	PITT, EIS	10^{-10}–10^{-7}	3.8–4.2 V	Dokko[24]
ESD film	GITT	10^{-13}–10^{-12}	N/A	Chen[46]
PLD film	GITT	1×10^{-10}	4.0–4.04 V	Striebel[47]
RF sp. film	GITT	10^{-11}	N/A	Birke[48]
Oxidation film	EIS, PITT	10^{-12}–10^{-8}	$0.7 < x < 1.0$	Sato[49]
PLD film	PITT	1×10^{-12}–4×10^{-11}	$0.5 < x < 0.95$	McGraw[50]
RF sp. film	PITT	10^{-11}–10^{-10}	$0.45 < x < 0.7$	Jang[51]
PLD film	EIS	1×10^{-11}–5×10^{-10}	$x = 0.7$	Iriyama[52]
RF sp., PLD film	GITT, EIS	10^{-14}–10^{-4}	$0.5 < x < 1.0$	Bouwman[53]
PLD film	EIS, PITT	2×10^{-12}–1×10^{-11}	$0.47 < x < 0.71$	Xia[15,54]
RF sp. film	PITT, EIS, GITT	10^{-12}–10^{-10}	$0.45 < x < 0.98$	Xie[55]
PLD film	PITT, EIS	6×10^{-13}–8×10^{-12}	3.85–4.20 V	Tang[56]
PLD epitaxial film	PITT	1×10^{-14}–2×10^{-12}	3.84–4.18 V	Shiraki[57]
PLD film	PITT	5×10^{-12}–2×10^{-10}	3.5–4.4 V	Matsuda[9]

We have developed a new technique to observe Li diffusion coefficients in electrode materials and solid electrolytes by combining isotope exchange and secondary ion mass spectrometry (SIMS).[29–32] The tracer diffusion coefficient (D^*) has been determined by analysing the distribution of Li isotopes. In particular, SIMS diffusion measurements have the following advantages: (1) application to electron–ion mixed conductors,[33] (2) determination of interfacial exchange rates and bulk diffusion coefficients,[34,35] and (3) application to grain boundary diffusion.[36,37] To the best of our knowledge, this is the first report of a SIMS based study of tracer diffusion in Li_xCoO_2.

In this study, we have conducted a detailed measurement on the composition dependence of D^* and $\tilde{D}$ in *c*-axis oriented Li_xCoO_2 thin films. We used a technique called the 'step-isotope-exchange method',[32] which enables the tracer diffusion measurements on thin-film electrodes even at room temperature. Instead of the space profile measurement used so far,[29,30] the time-dependence of the ^{6}Li isotope concentration in the Li_xCoO_2 thin film, which comes into contact with a ^{6}Li-enriched electrolyte to exchange Li ions, was measured. Furthermore, $\tilde{D}$ was obtained using an electrochemical method. The diffusion kinetics of *c*-axis oriented LCO thin films will be discussed by comparing $\tilde{D}$ and D^* and considering the effect of thermodynamic factors.

Methods

Sample preparation

Thin films of LCO were grown by pulsed laser deposition (PLD) as described in our previous papers.[4,7,9] The LCO thin films were deposited on Pt (200 nm)/Cr (10 nm) coated SiO_2 glass substrates using a $Li_{1.2}CoO_2$ pellet (TOSHIMA Manufacturing Co., Ltd) as a target in an oxygen atmosphere of 20 Pa with a substrate temperature of 500 °C. An ArF excimer laser (Coherent, COMPexPro 205) with a wavelength of 193 nm, a pulse energy of 200 mJ, a repetition rate of 15 Hz, and a fluence of 2 J cm^{-2} was used. The deposition time was 2.5 h. The thickness of the films was measured using a surface profilometer (Kosaka Laboratory, SE3000).

The thin films were characterized by X-ray diffraction (XRD), micro Raman spectroscopy, and inductively coupled plasma atomic emission spectroscopy (ICP-AES) composition analysis. The XRD patterns of Li_xCoO_2 thin films were recorded using an X-ray diffractometer (Rigaku, RINT-2100V) using CuK_α radiation. The 2θ scan range was $10°$–$90°$ at a scan rate of $2.0°\ min^{-1}$. The Raman spectra of the Li_xCoO_2 thin films were obtained using a micro-Raman spectrometer (Tokyo Instruments, Nanofinder30). A semiconductor laser, with a wavelength of 532 nm, was used for excitation at 2 μW output power. The composition of the $LiCoO_2$ thin film was analysed by ICP-AES (PerkinElmer, Optima 3300XL) by dissolving the thin films into aqua regia. The composition of the film was found to be $Co : Li = 1 : 1.03 \pm 0.02$. The chemical composition was found to be close to the stoichiometry of $LiCoO_2$.

The lithium composition (x) in the Li_xCoO_2 thin film was controlled electrochemically using a three-electrode beaker cell.[30,38] Metallic lithium was used as the counter and reference electrodes. The electrolyte used was 1 mol L^{-1} $LiClO_4$ in propylene carbonate (PC) (Tomiyama Pure Chemical Industries). The electrochemical measurements were performed using a potentiostat/galvanostat (Bio-Logic, VMP3). The potentiostatic intermittent titration technique (PITT) measurements were also performed using the three-electrode beaker cell. The applied potential step was 10 mV. The electric current as a function of time was measured for 1000 s.

The Li isotope ratio of the starting materials of LCO, Li and $LiClO_4$ was the natural abundance (^{nat}Li: 92.4% ^{7}Li and 7.6% ^{6}Li).

For the isotope ion-exchange, ^{6}Li-enriched $LiClO_4$ was synthesized according to a previously reported procedure.[32,58] An aqueous solution of $HClO_4$ (Wako Pure Chemical) was added dropwise to $^6Li_2CO_3$ (95% ^{6}Li, 5% ^{7}Li, Cambridge Isotope Laboratories. Inc.) until the white solid dissolved. The resultant $^6LiClO_4$ powder was vacuum dried at 200 °C. $^6LiClO_4$ was dissolved in PC (Kishida Chemical) in a glove box to obtain 1 mol L^{-1} $^6LiClO_4$/PC solution.[23]

Step-isotope-exchange method

A recently developed 'step-isotope-exchange method'[32] was used to measure the tracer diffusion coefficient. Fig. 1 shows an illustration of the step-isotope-exchange method. First, a part of the thin film was immersed in the solution for a time step, Δt. Then, an additional 0.5 mm of the sample was immersed for time, Δt. Repeating this procedure, the sample was divided into several regions with different ion exchange times. The isotope ratio, $^6Li/(^6Li + ^7Li)$, was determined by SIMS line analysis. A double focusing-type SIMS (CAMECA, IMS 7f) was used. The primary ion beam was composed of Cs^+ ions with a current of 1 nA and a voltage of 15 keV; the spot size of the focused ion beam was 1 μm. Point spacing of the line analysis was 100 μm and the analysis area was 10 × 10 μm^2. The isotope ratio was determined from the ratio of the intensities of ^{6}Li and ^{7}Li whose ionization efficiencies are the same.

The principles of the step-isotope-exchange method have been explained in detail in a previous paper,[32] so we will briefly describe them here. The isotope ratio in the Li_xCoO_2 thin film depends on the distance z from the surface and the time t.[23,59] Assuming the diffusion-controlled process, the isotope ratio in the film is described by the diffusion equation,

$$\frac{\partial C(z,t)}{\partial t} = D^* \frac{\partial^2 C(z,t)}{\partial z^2}, \tag{1}$$

where $C(z,t)$ is the concentration at a distance z, D^* is the tracer diffusion coefficient. In the step-isotope-exchange method, the isotope profile in the thickness direction is averaged due to the small thickness. The total amount of exchange isotopes $M(t)$ is obtained as,

$$\frac{M(t) - M_0}{M_s - M_0} = 1 - \sum_{n=0}^{\infty} \frac{8}{(2n+1)^2\pi^2} \exp\left(-\frac{(2n+1)^2\pi^2 D^* t}{4L^2}\right), \tag{2}$$

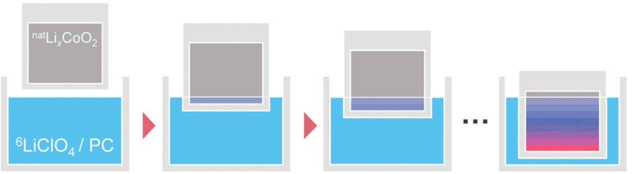

Fig. 1 Schematic of the step-isotope-exchange method. When the $^{nat}Li_xCoO_2$ thin film is immersed stepwise into the 1 mol L^{-1} $^6LiClO_4$/PC solution, ^{nat}Li is partly exchanged with ^{6}Li. After repeating this procedure, the sample is finally divided into several regions with different Li isotope ratios depending on the immersion times.

where M_0 is the initial isotope amount ($M_0 = C_0L$) and M_s is the amount after infinite time ($M_s = C_sL$). L is the thickness of the thin film, and n is an integer. The value of D^* was determined using this equation.

In general, the interfacial exchange-rate between the Li_xCoO_2 thin film and the electrolyte needs to be considered. The boundary condition of the diffusion equation is modified by including both the diffusion and the exchange-rate effects and the following solution is derived:[23,59]

$$\frac{C(z,t) - C_0}{C_s - C_0} = 1 - \sum_{n=1}^{\infty} \frac{2\Lambda \cos\left(\frac{b_n z}{L}\right) \exp\left(-\frac{b_n{}^2 D^* t}{L^2}\right)}{(b_n{}^2 + \Lambda^2 + \Lambda)\cos b_n}, \tag{3}$$

where Λ is a dimensionless parameter determined from an exchange rate k, the film thickness L, and the diffusion coefficient D^* as,

$$\Lambda = \frac{kL}{D^*}. \tag{4}$$

b_n is the n th positive root of the equation $b \tan b = \Lambda$. The large values of Λ are characteristic of the diffusion-controlled process. In contrast, in the case of the exchange-rate-controlled limit, it follows that

$$\frac{C(t) - C_0}{C_s - C_0} = 1 - \exp\left(-\frac{kt}{L}\right). \tag{5}$$

In this extreme case, there is no concentration gradient inside the thin film. Only the exchange rate k can be obtained from the isotope-exchange experiments.

PITT measurements

The chemical diffusion coefficient ($\tilde{D}$) was measured by PITT.[60,61] In the case of the diffusion-controlled process, under the assumptions required for PITT,[60,61] the time-dependent electric current $I(t)$ is found to be

$$I(t) = \frac{2\Delta Q\tilde{D}}{L^2} \sum_{n=1}^{\infty} \exp\left(-\frac{(2n-1)^2\pi^2\tilde{D}t}{4L^2}\right). \tag{6}$$

ΔQ is the total charge transfer during the voltage step.[61] The experimental data were fitted using eqn (6).

Considering the exchange-controlled case, the following equation is given as:[23]

$$I(t) = \frac{\tilde{k}\Delta Q}{L} \exp\left(-\frac{\tilde{k}t}{L}\right), \tag{7}$$

where $\tilde{k}$ is the chemical exchange rate. In this extreme case, only the chemical exchange rate $\tilde{k}$ can be obtained.

DFT calculations

To consider the probability of Li diffusion in LCO through the grain boundaries, we carried out DFT calculations using the Vienna *Ab initio* Simulation package (VASP).[62] The interaction between ions and electrons was described using the projector augmented wave (PAW) method. The wave function was expanded in plane waves using a 400 eV cut off and the

Brillouin zone was sampled at the Γ point. Exchange and correlation effects were incorporated within the generalized gradient approximation (GGA), using a Perdew–Burke–Ernzerhof gradient-corrected functional.[63] The aspherical contribution to the gradient corrections inside the PAW spheres was taken into account.[64] In all calculations, self-consistency was achieved with a tolerance of 10^{-3} eV Å^{-1} and 10^{-7} eV for the ionic and electronic loops, respectively. The migration of selected defects in LCO was studied using the climbing-image nudged elastic-band (NEB) method[65,66] with 5 images. A periodic supercell approach was used to model the antiphase boundaries (APBs). The (100) boundary was modelled in a $4 \times 4 \times 1$ ($4a$, $4b$, c) supercell of bulk LCO and the boundary is prepared by shifting the atoms in the half of the cell ($2 \times 4 \times 1$) to [0 0 0.5]. Here, $\boldsymbol{a}$, $\boldsymbol{b}$, and $\boldsymbol{c}$ are the lattice vectors of bulk LCO respectively.[67] All the calculated inner coordinates were optimized in the experimental lattice parameters. The (110) boundary was modelled in a $2 \times 4 \times 1$ supercell of new basis vector of ($\boldsymbol{a} - \boldsymbol{b}$, $\boldsymbol{a} + \boldsymbol{b}$, $\boldsymbol{c}$) and the boundary was prepared by shifting half of the cell ($2 \times 2 \times 1$) to [0 0 0.5].

Results and discussion

Characterization of the Li$_x$CoO$_2$ thin films

Fig. 2 shows the electrochemical properties of the LCO thin films obtained by PITT. The characteristic features of LCO thin films obtained were found to be consistent with previous reports.[4,9] The potential *vs.* composition plot (coulometric titration curve) was obtained by integrating the incremental capacities ($\Delta Q/\Delta V$). The method of obtaining the potential *vs.* Li composition plot from the PITT experiment was performed according to that of Jang *et al.*[51] The data are normalized so that the minimum of $\Delta Q/\Delta V$ falls at $x = 0.5$ corresponding to $V = 4.14$ V and $x = 1.0$ corresponding to $V = 3.82$ V, based on the phase diagram of Li$_x$CoO$_2$.[1] The incremental capacitance indicates a large peak at 3.9 V corresponding to the first-order transition between the two hexagonal phases (H1 and H2). Above 4 V, the incremental capacitance shows two small peaks associated with the order/disorder transition at compositions close to Li$_{0.5}$CoO$_2$.[1,51]

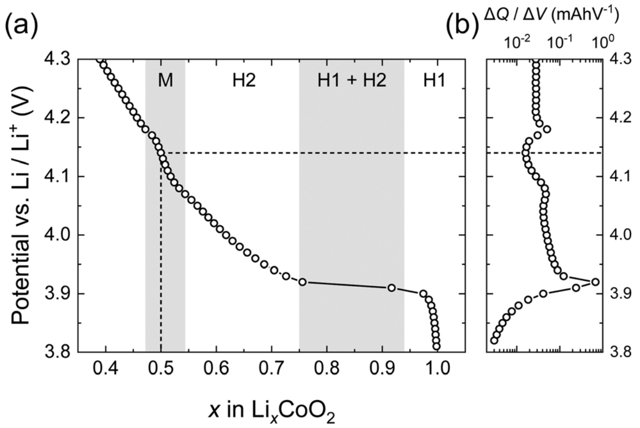

Fig. 2 Electrochemical properties of Li$_x$CoO$_2$ thin films obtained by PITT: (a) potential *vs.* Li composition x plot, and (b) incremental capacity ($\Delta Q/\Delta V$) *vs.* potential. The data are normalized so that the minimum in $\Delta Q/\Delta V$ falls at $x = 0.5$ based on the phase diagram of Li$_x$CoO$_2$.

Fig. 3(a) shows *ex situ* XRD patterns of the LCO thin films. Highly (003) oriented XRD patterns were observed, which confirm the *c*-axis orientation of the LCO thin films. As the maintained potential increased, the *c*-axis lattice parameter of the Li$_x$CoO$_2$ thin films increased. The *c*-axis lattice constant of the as-prepared LCO film was 14.04 Å, which then increases up to 14.37 Å at 4.15 V. The variation of the lattice parameter was in good agreement with values of the bulk LCO reported in the literature,[1,2] as shown in Fig. 3(b).

Fig. 4(a) shows the *ex situ* Raman spectra of Li$_x$CoO$_2$ thin films. The Raman active modes of LCO were observed at 595 cm^{-1} (A_{1g}) and 486 cm^{-1} (E_g), respectively. As the potential increases, the Raman peaks shift to lower wave numbers and decrease in intensity. These results are in good agreement with previous reports for Li$_x$CoO$_2$ by *ex situ*[3] and *in situ*[4] Raman spectroscopy as shown in Fig. 4(b). In addition, small peaks due to Co$_3$O$_4$ were identified at 520 cm^{-1} (T_{2g}) and 690 cm^{-1} (A_{1g}), which was attributed to the trace amount of cobalt oxide near the substrates.[4]

Tracer diffusion coefficient of the Li$_x$CoO$_2$ thin films

Fig. 5 shows the SIMS line profile of the Li$_{0.84}$CoO$_2$ thin film prepared by the step-isotope-exchange method. The Li composition

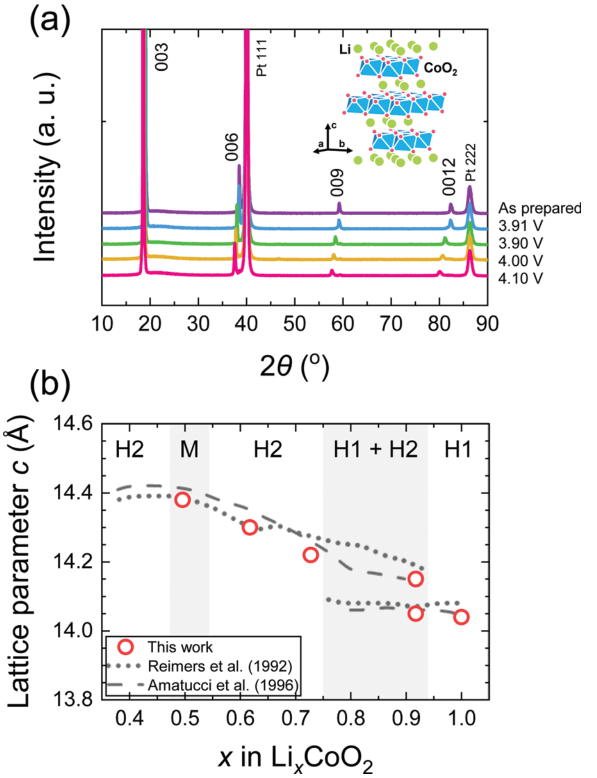

Fig. 3 (a) *Ex situ* XRD pattern of Li$_x$CoO$_2$ thin films with a schematic of the crystal structure of LiCoO$_2$ and (b) the *c*-axis lattice parameter compared with literature data. The samples were prepared at 3.91, 3.93, 4.00 and 4.15 V, respectively. As the potential increases, the *c*-axis lattice parameter increases. The change in the lattice parameters is in good agreement with values of the bulk LCO reported in the literature.[1–4]

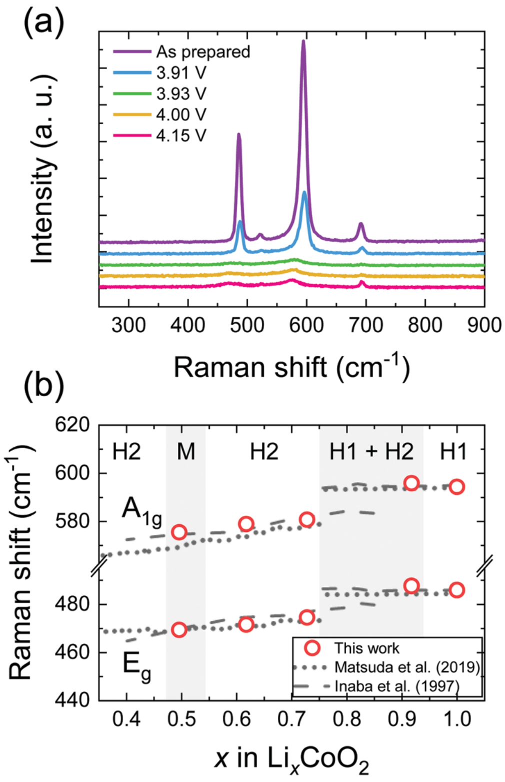

Fig. 4 (a) *Ex situ* micro Raman spectra and (b) Raman shift of Li_xCoO_2 thin films. The samples were prepared at 3.91, 3.93, 4.00 and 4.15 V, respectively. As the potential increases, A_{1g} and E_g modes of LCO thin films shifted to a lower wavenumber and decreased in intensity. The peak position of Co_3O_4 does not change, as it is electrochemically inactive. The changes in the Raman shifts of A_{1g} and E_g modes were in good agreement with values reported in the literature.

$x = 0.84$ was determined from the potential–composition plot at 3.915 V. A stepwise change in the isotope ratio after 0.5 mm intervals is observed. At each step position, the isotope exchange time varies by $\Delta t = 360$ s. The position was converted to the ion-exchange time, and eqn (2) was used to fit the experimental data. The theoretical curve assuming the diffusion control was in good agreement with the experiment, which gives the tracer diffusion coefficient of Li to be $D^* = 4.9 \times 10^{-13}$ cm^2 s^{-1} at $x = 0.84$.

Fig. 6 shows the results of the step-isotope-exchange method for different compositions. The results were analysed for both diffusion-controlled and exchange-rate-controlled cases. For compositions $0.98 > x > 0.92$, the data were fitted better by the diffusion-controlled form of eqn (2). For fast diffusion cases ($0.72 > x > 0.50$), both eqn (2) and (5) agree with the experimental data.

As discussed in the next paragraph, k is estimated to be fast. Therefore, the diffusion-controlled condition is also valid for the composition of $0.72 > x > 0.50$. Hence, the diffusion coefficients can be determined from the step-isotope-exchange experiments and eqn (2). Table 2 summarizes the D^* values determined from these experiments.

Here, we estimate the parameter Λ to evaluate the dominant process. The isotope exchange rate k is related to the exchange current density i_0 by $i_0 = FC_0k$,[23,34] where C_0 is the molar concentration of Li in LCO, which is 0.055 mol cm^{-3} at stoichiometry. The value of i_0 can be estimated from the charge-transfer resistance (R_{ct}) *via* the Butler–Volmer equation. In the literature, the values of R_{ct} = 7–14 Ω cm^2 have been reported for Li_xCoO_2 thin films at 4.0 V,[52] where the Li composition x is 0.6. The exchange rate k is, therefore, estimated to be 0.6–1 × 10^{-6} cm s^{-1}. If the thickness L is 500 nm and D^* is 1 × 10^{-12} cm^2 s^{-1}, then the parameter Λ is calculated to be 30–60. Thus, the diffusion-controlled condition ($\Lambda > 10$) is

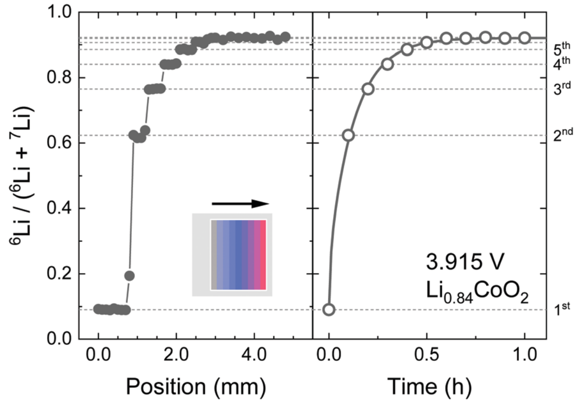

Fig. 5 SIMS analysis of the $Li_{0.84}CoO_2$ thin film prepared by the step-isotope-exchange method; (left) isotope profile measured by line analysis, and (right) time evolution of the isotope ratio. The solid line shows the fitting curve using eqn (2). The parameters for fitting were as follows; $C_0 = 0.08$, $C_s = 0.95$, $D^* = 4.9 \times 10^{-13}$ cm^2 s^{-1}, and $L = 240$ nm.

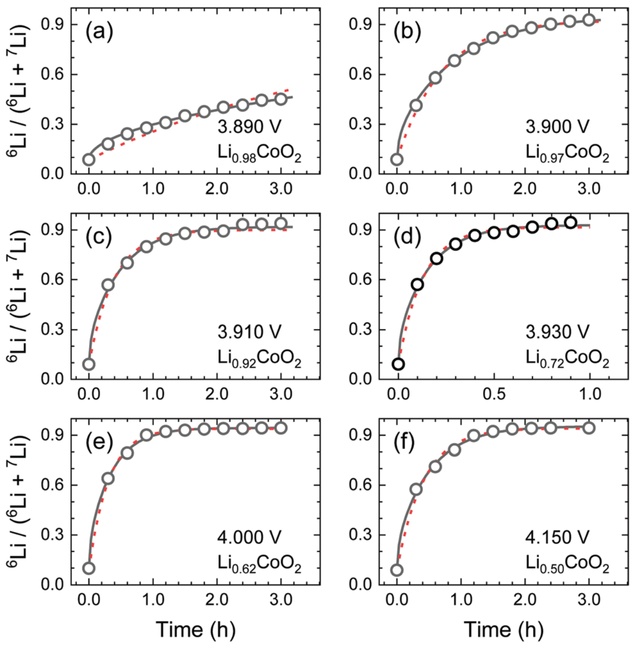

Fig. 6 Ion-exchange time dependence of the $^6Li/(^6Li + ^7Li)$ isotope ratio in the Li_xCoO_2 thin films: (a–f) correspond to x = 0.98, 0.97, 0.92, 0.73, 0.62, and 0.50, respectively. The black solid lines show fitting curves for the diffusion-controlled case using eqn (2). The red broken lines indicate the exchange-rate controlled case using eqn (5).

Table 2 Tracer diffusion coefficients D^* of the Li_xCoO_2 thin films obtained by the step-isotope-exchange experiments. The values of D^* were obtained from eqn (2) assuming the diffusion control

Potential (V)	x in Li_xCoO_2	Phase	Thickness (nm)	D^* ($cm^2\ s^{-1}$)
4.230	0.437	H2	320	7.2×10^{-13}
4.151	0.496	M	690	1.0×10^{-12}
4.050	0.566	H2	430	1.7×10^{-12}
4.002	0.616	H2	690	1.5×10^{-12}
3.970	0.656	H2	280	7.0×10^{-13}
3.931	0.725	H2	290	5.7×10^{-13}
3.930	0.726	H2	660	1.1×10^{-12}
3.915	0.834	H1 + H2	420	3.5×10^{-13}
3.915	0.843	H1 + H2	240	4.9×10^{-13}
3.910	0.917	H1	560	6.9×10^{-13}
3.905	0.945	H1	460	4.7×10^{-13}
3.905	0.944	H1	470	2.3×10^{-13}
3.900	0.973	H1	460	2.5×10^{-13}
3.890	0.984	H1	350	1.6×10^{-14}

satisfied. The assumption of diffusion control is found to be more plausible.

In the vicinity of the stoichiometric composition, the values of D^* become significantly low. In this case, the conventional depth profile analysis[68,69] can be applied. Fig. 7 shows the SIMS depth profile of Li_xCoO_2 thin films (x = 0.995 and 0.999). We analysed the depth profile by assuming a semi-infinite solution of the diffusion equation considering both diffusion and exchange:[59]

$$\frac{C(z,t)-C_0}{C_s-C_0} = \mathrm{erfc}\left(\frac{z}{2\sqrt{D^*t}}\right) - \exp\left(hz+h^2D^*t\right)\mathrm{erfc}\left(\frac{z}{2\sqrt{D^*t}}+h\sqrt{D^*t}\right), \qquad (8)$$

where $h = k/D^*$ is the ratio of the exchange rate k to D^*. The depth profile was fitted using a diffusion coefficient D^* and an exchange rate k. The parameters are summarized in Table 3. The D^* was found to be very small, $3 \times 10^{-17}\ cm^2\ s^{-1}$, at 20 °C. The activation energy of D^* was approximately 0.25 ± 0.1 eV. Note that the baseline was greater than the natural abundance (^6Li: 7.6%), suggesting the presence of a fast diffusion component, such as grain-boundary diffusion or *ab*-plane diffusion owing to a local disturbance in the film orientation.

Fig. 8 shows D^* as a function of x in the Li_xCoO_2 thin films. For the composition near stoichiometry ($0.94 < x < 1.0$), the value of D^* drastically changes from 10^{-17} to $10^{-13}\ cm^2\ s^{-1}$. This behaviour can be explained by the vacancy diffusion mechanism. In the vacancy diffusion mechanism, the Li^+ ions can jump only when the neighbouring site is vacant. Then, D^* is proportional to the probability of the vacant Li site, *i.e.* $(1-x)$. Therefore, D^* can be written as,[14,32]

$$D^* = (1-x)\rho d^2\Gamma = D_0(1-x), \qquad (9)$$

where ρ is a geometric factor that depends on the symmetry of the sublattice, d is the jump distance between adjacent sites, Γ is the jump frequency, and $(1-x)$ is the vacancy blocking factor. The broken line in Fig. 8 shows the curve using eqn (9), where $D_0 = \rho d^2\Gamma$ is assumed to be constant. Notably, the value of D^* obtained in this experiment represents the diffusion coefficients for *c*-axis diffusion, which are expected to be lower than those for the axis parallel to the *ab*-plane. In fact, NMR and muon-spin relaxation experiments[27,28] have reported much higher diffusion coefficients, for example, $7 \times 10^{-10}\ cm^2\ s^{-1}$ at 300 K for muon-spin relaxation experiments using the $Li_{0.73}CoO_2$ powder.[28] It is surprising that D^* is extremely low near the stoichiometric composition, given that the $LiCoO_2$ thin film is readily deintercalated by charging in an electrochemical cell. As we will describe later, the chemical diffusion coefficient, $\tilde{D}$, which determines Li deintercalation rate, is almost unchanged. This is because the vacancy blocking factor is cancelled by the thermodynamic factor due to the effect of entropy.

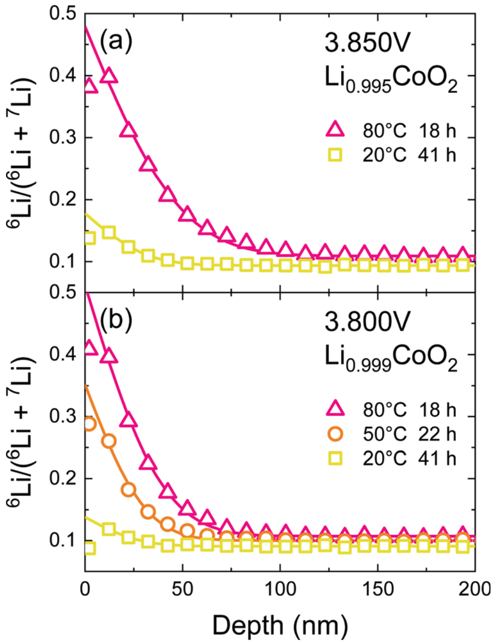

Fig. 7 SIMS depth profile of the Li_xCoO_2 thin film (x = 0.995 and 0.999). The potential of the sample was kept at 3.85 or 3.80 V for 12 h. Then, isotope ion-exchange was carried out in $^6LiClO_4$/PC solution. Solid lines show the fitting curve based on eqn (8).

Table 3 Tracer diffusion coefficient D^* and exchange rate k of the Li_xCoO_2 thin films obtained by the SIMS depth profile. The parameters were obtained by fitting based on eqn (8)

Potential (V)	x in Li_xCoO_2	Temp. (°C)	Diff. time (h)	D^* ($cm^2\ s^{-1}$)	k ($cm\ s^{-1}$)
3.85	0.995	80	18	1.6×10^{-16}	3.3×10^{-11}
3.85	0.995	20	41	3.0×10^{-17}	1.5×10^{-12}
3.80	0.999	80	18	9.7×10^{-17}	3.1×10^{-11}
3.80	0.999	40	22	5.1×10^{-17}	9.8×10^{-12}
3.80	0.999	20	41	3.0×10^{-17}	7.5×10^{-13}

Model of *c*-axis diffusion in the Li_xCoO_2 thin film

In the layered LCO, in-plane diffusion is expected to be fast, but diffusion through the layers is unlikely to occur. Direct penetration through the CoO_2 sheet has a significantly high energy barrier

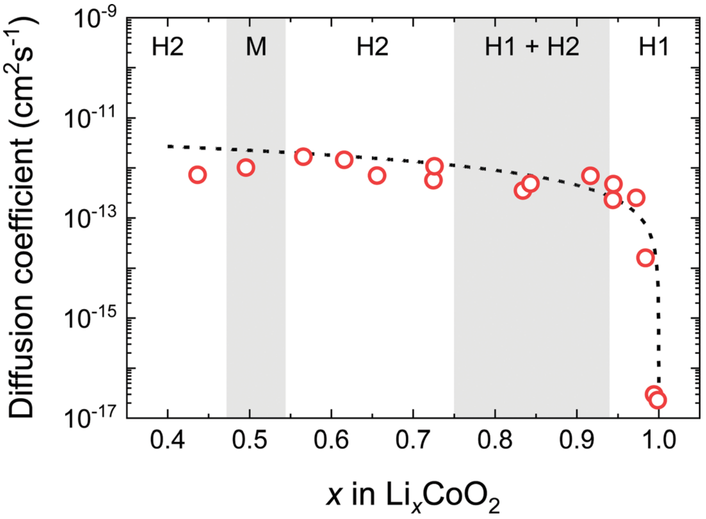

Fig. 8 Composition dependence of the tracer diffusion coefficient D^* of Li_xCoO_2 thin films. Open red circles correspond to D^* in the c-axis direction. The broken line shows the curve of eqn (9) based on the vacancy diffusion mechanism.

(6.8 eV).[21] Therefore, we propose a model to explain the Li^+ ion diffusion in the c-axis, as shown in Fig. 9. This model assumes that Li^+ ions can diffuse through the possible antiphase boundaries (APBs) or the defects in the CoO_2 layer. Continuous diffusion through the same APB is prevented because the APB will be periodically blocked by the CoO_2 layer. For the long-range c-axis transport, the Li^+ ions need to move from one APB to another APB through diffusion parallel to the *ab*-plane. Even in the case of anti-site defects in the CoO_2 layer, the Li^+ ions would move from one defect to another through *ab*-plane diffusion. As a result, Li^+ ions diffuse along the c-axis through the CoO_2 layer. Here, the length of the Li^+ ion diffusion is much longer than the c-axis distance. Hence, the diffusion coefficient will be much smaller than the direct penetration. This model can explain the behaviour of observed D^* proportional to the vacancy concentration because the c-axis diffusion (D^*) depends on the *ab*-plane diffusion (D_{ab}). The model also explains the small E_a, despite the low value of D^*, because the E_a reflects the migration barrier in the *ab* plane.

To validate the models mentioned above, we performed DFT calculations for the diffusion of Li^+ ions in the possible defects.

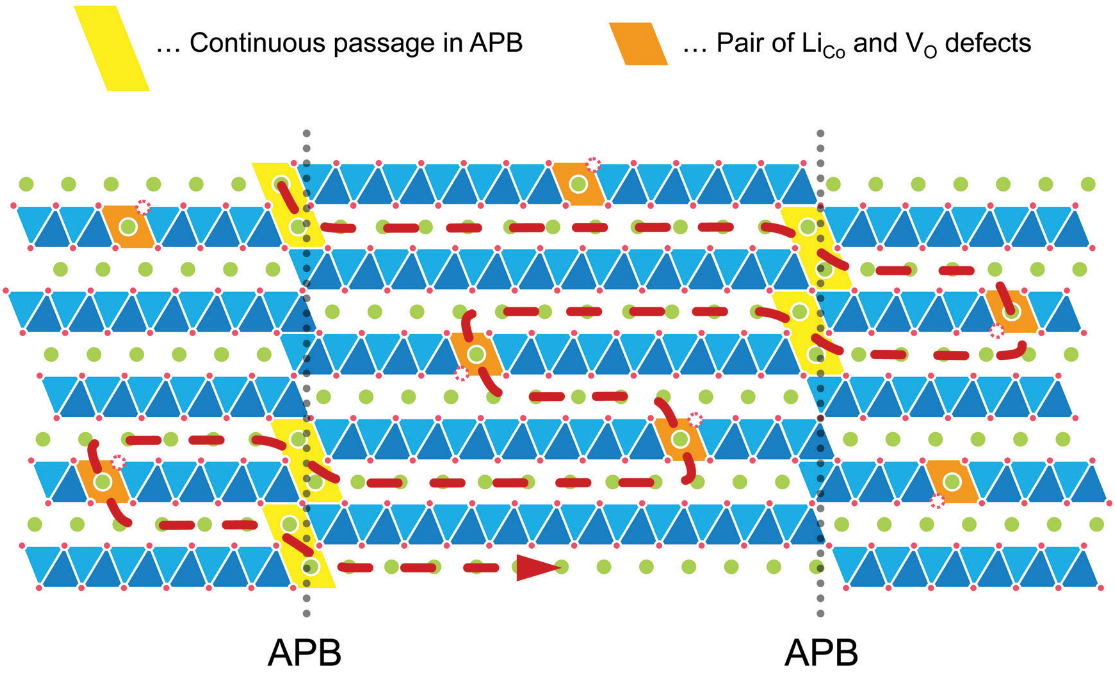

Fig. 9 Schematic model of c-axis diffusion in the LCO thin films. This model assumes that Li^+ ions can diffuse through the antiphase boundaries (APBs) or the defects in the CoO_2 layer. For the long-range c-axis transport, the Li^+ ions need to move from one defect to another defect through diffusion parallel to the *ab* plane. The length of the Li^+ ion diffusion becomes much longer than the c-axis distance.

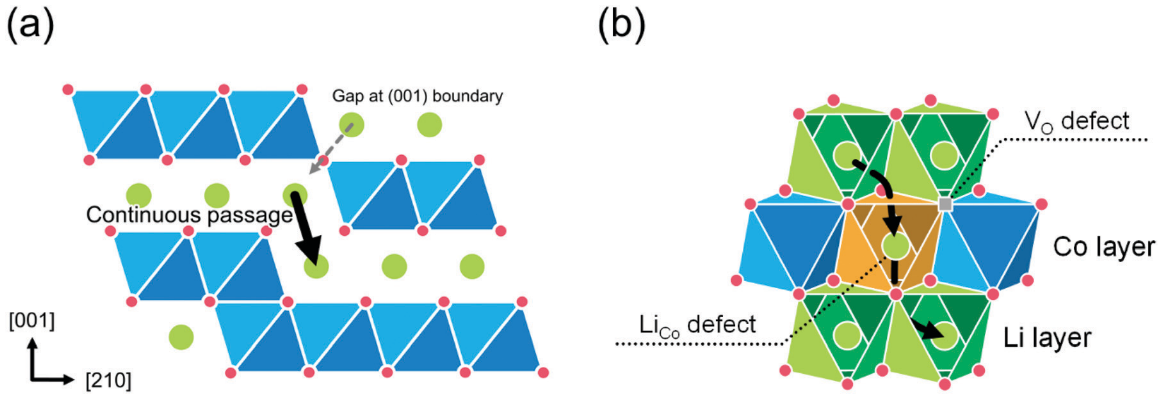

Fig. 10 Schematic models of defects for *c*-axis diffusion in the LCO thin films: (a) a model of the APB along (100) plane and (b) a model for the pair of Li_{Co} and V_O defects in the CoO_2 layer.

First, the diffusion along the *ab*-plane direction was calculated. The results show that the migration energy barrier is 0.7 eV for the single vacancy and 0.3 eV for the divacancy models. These values are in good agreement with previous reports.[12,13]

Next, the diffusion through the APB was calculated. The APB structure is understood as a stacking fault with a relative displacement of a 1/2 unit cell along the [001] direction. Fig. 10(a) shows a schematic of the (100) boundary. The calculation results show that the (100) and (110) boundaries are stable with a low formation energy of 0.08 eV Å^{-2}, and 0.05 eV Å^{-2}, respectively (consistent with the literature[21]). The continuous downward passage in the (100) boundary shows a relatively low energy barrier, which is 0.9 eV for single vacancy and 0.6 eV for divacancy models. However, it should be noted that the diffusion in the (100) boundary is interrupted by the CoO_2 block, which periodically appears in the (100) boundary. The migration energy barrier for (110) boundary is 0.9 eV for the single vacancy model. The divacancy model cannot function in the (110) boundary.

Finally, the diffusion through defects in the CoO_2 layer was calculated. The defect model was proposed by Levasseur *et al.*[70] for the lithium overstoichiometric samples, where the excess Li replace the cobalt ions (antisite defects, Li_{Co}), and the charge is compensated by oxygen vacancies (V_O). Fig. 10(b) shows a schematic of the pair of Li_{Co} and V_O defects in the CoO_2 layer. The calculated energy barriers through the pair of defects are 1.0 eV for single vacancy, 0.5 eV for divacancy, and 0.4 eV for triple vacancy models, respectively. The diffusion energy barrier through a pair of Li_{Co} and V_O defects shows a sharp decrease in the energy for Li^+ ions to cross the CoO_2 sheet.

The DFT calculations show that Li^+ ions can penetrate the CoO_2 layer through these defects. However, due to the small number of defects, the probability is low. Therefore, Li^+ ions will diffuse longer distances, resulting in the lower diffusion coefficient. These models explain well the values of D^* along the *c*-axis obtained by the tracer diffusion experiments.

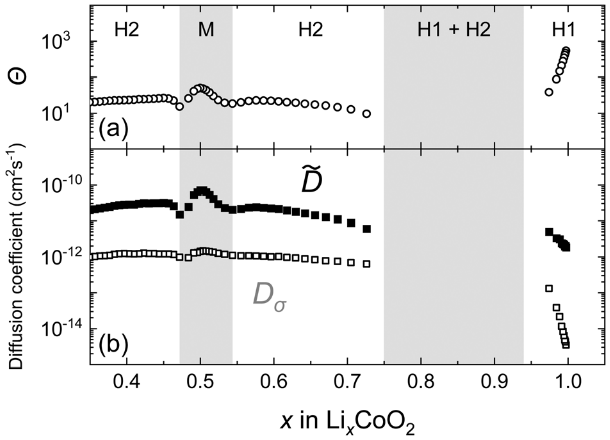

Fig. 11 Li composition x dependence of the thermodynamic factors (Θ), chemical diffusion coefficients ($\tilde{D}$), and conductivity diffusion coefficients (D_σ) for Li_xCoO_2 thin films measured by PITT.

Comparison of tracer and chemical diffusion coefficients

Fig. 11 shows the chemical diffusion coefficient $\tilde{D}$ of the Li_xCoO_2 thin film obtained by PITT. The composition dependence of $\tilde{D}$ is different from that of D^* because of the following reasons: (1) the decrease in the $\tilde{D}$ near the stoichiometric composition ($x = 1$) is small, (2) the $\tilde{D}$ shows a maximum value at the M phase ($x = 0.5$), and (3) the value of $\tilde{D}$ shows two local minima at $x = 0.53$ and 0.48, which are associated with the order/disorder transitions near $Li_{0.5}CoO_2$. These behaviours are in good agreement with previous studies.[9,51] Note that in the two-phase coexistence region, the measurement of $\tilde{D}$ by PITT is difficult because of the transient behaviour in the two different phases.

Since the driving force for diffusion is the chemical potential of Li (μ_{Li}), $\tilde{D}$ is enhanced by a thermodynamic factor Θ. According to the theory for the mixed conductors,[60] the following relationship holds for:

$$\tilde{D} = \Theta D_\sigma, \tag{10}$$

where D_σ is the conductivity diffusion coefficient (or component diffusion coefficient), which is derived from the mobility of Li^+ ions through the Nernst–Einstein equation. Assuming that Li_xCoO_2 is predominantly an electronic conductor, Θ can be written as:[51,71]

$$\Theta = \frac{C_{Li}}{k_B T}\frac{d\mu_{Li}}{dC_{Li}}, \tag{11}$$

where C_{Li} is the concentration of Li, k_{B} is the Boltzmann constant, and T is the absolute temperature. Using the relation between the electrode potential E (*vs.* Li/Li^{+}) and the chemical potential, $\mu_{\mathrm{Li}} = -eE$, the equation can be written as,

$$\Theta = -\frac{ex}{k_{\mathrm{B}}T}\frac{\mathrm{d}E}{\mathrm{d}x}, \quad (12)$$

where e is the elementary charge, and x is the relative concentration of Li in Li$_x$CoO$_2$. From this equation Θ can be experimentally determined.

The composition dependence of Θ in the Li$_x$CoO$_2$ thin films is also shown in Fig. 11. Θ shows a large value where the slope of the composition-OCV curve is large. Near the stoichiometric composition, Θ increases significantly up to 10^3. Thus, $\tilde{D}$ is greatly enhanced near the stoichiometry. In an ideal intercalation compound (*i.e.*, a lattice gas model with non-interacting particles[72]), the thermodynamic factor is represented as $\Theta = 1/(1 - x)$,[72,73] which is derived from the entropy term. Therefore, the large value of Θ near stoichiometric composition is reasonable. The constant values of $\tilde{D}$ in the H1 phase are attributed to the cancellation of the thermodynamic and the vacancy blocking factors.

Fig. 12 shows the composition dependence of D_σ obtained from PITT using eqn (10) and that of D^* obtained from SIMS experiments. The values of D^* and D_σ agree well in the compositional range of $0.45 < x < 1.0$. The composition dependence of D_σ is also consistent with the vacancy diffusion mechanism shown by the solid dashed line. In the *c*-axis diffusion coefficient of Li$_x$CoO$_2$, $D_\sigma \approx D^*$ is clearly demonstrated.

Finally, we discuss the large discrepancy in the reported $\tilde{D}$ in Table 1 obtained by the electrochemical methods. There are two main reasons for this: (1) the influence of the surface exchange rates and (2) the effect of the anisotropy of the diffusion coefficient characteristic in LCO. If the interfacial resistance is too large, the index Λ in eqn (4) is dominated by k. Then, the *I*–*t* curve in the PITT experiment shows the exponential decay as eqn (7), which is indistinguishable from the long-time domain of the diffusion-controlled case. As a result, small apparent D would be observed. In addition, considerably fast diffusion is also challenging to be measured. Assuming L of 1 μm and k of 10^{-6} cm s^{-1}, D should be less than 10^{-11} cm^2 s^{-1} to satisfy the conditions for $\Lambda > 10$. To measure faster D, L needs to be further increased. Another reason is the anisotropic diffusion in LCO. The $\tilde{D}$ values reported for the powder samples (10^{-10}–10^{-8} cm^2 s^{-1})[5,39–42] are several orders of magnitude higher than those for the *c*-axis oriented thin films (10^{-14}–10^{-10} cm^2 s^{-1}),[9,15,50,52,54,56,57] which must be the effect of *ab*-plane diffusion. However, in the case of powder electrodes, the diffusion length may be misidentified due to solution immersion, and the value of $\tilde{D}$ will be overestimated. Single-crystal electrodes will provide a well-defined geometry, though they are not easily available. If suitable sized single crystals are available, direct evidence of *ab*-plane diffusion in Li$_x$CoO$_2$ can be obtained by the tracer diffusion technique. We are currently studying *ab*-plane diffusion using LCO single crystals, which will be published in the near future.

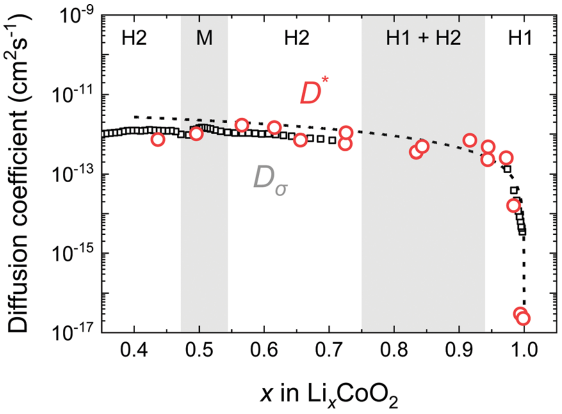

Fig. 12 Comparison of D^* and D_σ of the Li$_x$CoO$_2$ thin films. D^* and D_σ are plotted as open circles and open squares, respectively. The composition dependence of D_σ was measured by PITT and corrected by thermodynamic factors. The broken line shows the vacancy diffusion model. The values of D_σ and D^* agree well in the wide range of compositions.

Conclusions

The tracer diffusion coefficient D^* of the *c*-axis oriented Li$_x$CoO$_2$ thin films was investigated by the step-isotope-exchange method in conjunction with SIMS analysis. The isotope exchange method has enabled us to investigate the tracer diffusion and interfacial exchange rate in the cathode materials of Li-ion batteries. The D^* values for the *c*-axis direction ranged from 10^{-17} to 10^{-12} cm^2 s^{-1} for the *c*-axis oriented Li$_x$CoO$_2$ thin films ($0.4 < x < 1.0$). DFT calculations showed the low migration energy barrier for diffusion of Li$^+$ ions through the APBs or defects in the CoO$_2$ layer. The *c*-axis diffusion of Li$^+$ ions occurs from one layer to another layer through these defects in the LCO thin films. The composition dependence of D^* is explained by the vacancy diffusion mechanism. The conductivity diffusion coefficient D_σ obtained by PITT experiments was found to be in good agreement with D^* over a wide range of compositions. The ion-exchange SIMS technique is suitable for studying lithium-ion battery materials, especially electron–ion mixed conductors.

Conflicts of interest

There are no conflicts to declare.

Acknowledgements

This work was supported by JSPS KAKENHI, Grant Numbers 17K19134 and 19H05814. For the SIMS experiment, we thank the ‘Center for Fusion Research of Nano-Interface Devices, Tohoku University’ of ‘Low-Carbon Research Network’ funded by MEXT (Ministry of Education, Culture, Sports, Science and Technology), Japan. The SIMS measurements were also performed at the National Institute for Materials Science (NIMS)

Battery Research Platform. The computation in this study was performed on Numerical Materials Simulator at NIMS. This study was also supported by the JST ALCA-SPRING (Specially Promoted Research for Innovative Next Generation Batteries) Project, Grant Number JPMJAL1301.

Notes and references

1 J. N. Reimers and J. R. Dahn, *J. Electrochem. Soc.*, 1992, **139**, 2091–2097.
2 G. G. Amatucci, *J. Electrochem. Soc.*, 1996, **143**, 1114.
3 M. Inaba, Y. Iriyama, Z. Ogumi, Y. Todzuka and A. Tasaka, *J. Raman Spectrosc.*, 1997, **28**, 613–617.
4 Y. Matsuda, N. Kuwata, T. Okawa, A. Dorai, O. Kamishima and J. Kawamura, *Solid State Ionics*, 2019, **335**, 7–14.
5 K. Mizushima, P. C. Jones, P. J. Wiseman and J. B. Goodenough, *Mater. Res. Bull.*, 1980, **15**, 783–789.
6 J. M. Tarascon and M. Armand, *Nature*, 2001, **414**, 359–367.
7 N. Kuwata, N. Iwagami, Y. Tanji, Y. Matsuda and J. Kawamura, *J. Electrochem. Soc.*, 2010, **157**, A521–A527.
8 N. Kuwata, J. Kawamura, K. Toribami, T. Hattori and N. Sata, *Electrochem. Commun.*, 2004, **6**, 417–421.
9 Y. Matsuda, N. Kuwata and J. Kawamura, *Solid State Ionics*, 2018, **320**, 38–44.
10 J. Bates, *Solid State Ionics*, 2000, **135**, 33–45.
11 K. Takada, *Acta Mater.*, 2013, **61**, 759–770.
12 A. Van der Ven and G. Ceder, *Electrochem. Solid-State Lett.*, 2000, **3**, 301–304.
13 A. Van der Ven, G. Ceder, M. Asta and P. D. Tepesch, *Phys. Rev. B: Condens. Matter Mater. Phys.*, 2001, **64**, 184307.
14 A. Van der Ven, J. Bhattacharya and A. A. Belak, *Acc. Chem. Res.*, 2013, **46**, 1216–1225.
15 H. Xia and L. Lu, *Electrochim. Acta*, 2007, **52**, 7014–7021.
16 S. Shiraki, T. Shirasawa, T. Suzuki, H. Kawasoko, R. Shimizu and T. Hitosugi, *ACS Appl. Mater. Interfaces*, 2018, **10**, 41732–41737.
17 H. Moriwake, A. Kuwabara, C. A. J. Fisher, R. Huang, T. Hitosugi, Y. H. Ikuhara, H. Oki and Y. Ikuhara, *Adv. Mater.*, 2013, **25**, 618–622.
18 P.-V. Ong, Z. Yang, P. V. Sushko and Y. Du, *J. Phys. Chem. Lett.*, 2018, **9**, 5515–5520.
19 N. Balke, S. Jesse, A. N. Morozovska, E. Eliseev, D. W. Chung, Y. Kim, L. Adamczyk, R. E. García, N. Dudney and S. V. Kalinin, *Nat. Nanotechnol.*, 2010, **5**, 749–754.
20 N. Balke, S. Kalnaus, N. J. Dudney, C. Daniel, S. Jesse and S. V. Kalinin, *Nano Lett.*, 2012, **12**, 3399–3403.
21 X. Zhu, C. S. Ong, X. Xu, B. Hu, J. Shang, H. Yang, S. Katlakunta, Y. Liu, X. Chen, L. Pan, J. Ding and R.-W. Li, *Sci. Rep.*, 2013, **3**, 1084.
22 M. Park, X. Zhang, M. Chung, G. B. Less and A. M. Sastry, *J. Power Sources*, 2010, **195**, 7904–7929.
23 C. Montella, *J. Electroanal. Chem.*, 2002, **518**, 61–83.
24 K. Dokko, M. Mohamedi, Y. Fujita, T. Itoh, M. Nishizawa, M. Umeda and I. Uchida, *J. Electrochem. Soc.*, 2001, **148**, A422–A426.
25 M. Hayashi, M. Takahashi and Y. Sakurai, *J. Power Sources*, 2007, **174**, 990–995.
26 T. Hayashi, J. Okada, E. Toda, R. Kuzuo, Y. Matsuda, N. Kuwata and J. Kawamura, *J. Power Sources*, 2015, **285**, 559–567.
27 K. Nakamura, H. Ohno, K. Okamura, Y. Michihiro, T. Moriga, I. Nakabayashi and T. Kanashiro, *Solid State Ionics*, 2006, **177**, 821–826.
28 J. Sugiyama, K. Mukai, Y. Ikedo, H. Nozaki, M. Månsson and I. Watanabe, *Phys. Rev. Lett.*, 2009, **103**, 147601.
29 N. Kuwata, X. Lu, T. Miyazaki, Y. Iwai, T. Tanabe and J. Kawamura, *Solid State Ionics*, 2016, **294**, 59–66.
30 N. Kuwata, M. Nakane, T. Miyazaki, K. Mitsuishi and J. Kawamura, *Solid State Ionics*, 2018, **320**, 266–271.
31 M. Kato, T. Hayashi, G. Hasegawa, X. Lu, T. Miyazaki, Y. Matsuda, N. Kuwata, K. Kurihara and J. Kawamura, *Solid State Ionics*, 2017, **308**, 54–60.
32 N. Kuwata, G. Hasegawa, D. Maeda, N. Ishigaki, T. Miyazaki and J. Kawamura, *J. Phys. Chem. C*, 2020, **124**, 22981–22992.
33 T. Ishigaki, S. Yamauchi, J. Mizusaki, K. Fueki and H. Tamura, *J. Solid State Chem.*, 1984, **54**, 100–107.
34 B. Steele, J. Kilner, P. Dennis, A. McHale, M. Vanhemert and A. Burggraaf, *Solid State Ionics*, 1986, **18-19**, 1038–1044.
35 R. De Souza, *Solid State Ionics*, 1998, **106**, 175–187.
36 A. Berenov, *Solid State Ionics*, 1999, **122**, 41–49.
37 K. Watanabe, I. Sakaguchi, S. Hishita, N. Ohashi and H. Haneda, *Appl. Phys. Express*, 2011, **4**, 055801.
38 N. Kuwata, R. Kumar, K. Toribami, T. Suzuki, T. Hattori and J. Kawamura, *Solid State Ionics*, 2006, **177**, 2827–2832.
39 A. Honders, J. M. der Kinderen, A. H. van Heeren, J. H. W. de Wit and G. H. J. Broers, *Solid State Ionics*, 1985, **15**, 265–276.
40 M. G. S. R. Thomas, P. G. Bruce and J. B. Goodenough, *Solid State Ionics*, 1985, **17**, 13–19.
41 Y.-M. Choi, S.-I. Pyun, J.-S. Bae and S.-I. Moon, *J. Power Sources*, 1995, **56**, 25–30.
42 J. Barker, R. Pynenburg, R. Koksbang and M. Y. Saidi, *Electrochim. Acta*, 1996, **41**, 2481–2488.
43 D. Aurbach, M. D. Levi, E. Levi, H. Teller, B. Markovsky, G. Salitra, U. Heider and L. Heider, *J. Electrochem. Soc.*, 1998, **145**, 3024–3034.
44 M. D. Levi, G. Salitra, B. Markovsky, H. Teller, D. Aurbach, U. Heider and L. Heider, *J. Electrochem. Soc.*, 1999, **146**, 1279–1289.
45 M. Okubo, Y. Tanaka, H. Zhou, T. Kudo and I. Honma, *J. Phys. Chem. B*, 2009, **113**, 2840–2847.
46 C. H. Chen, A. A. J. Buysman, E. M. Kelder and J. Schoonman, *Solid State Ionics*, 1995, **80**, 1–4.
47 K. A. Striebel, C. Z. Deng, S. J. Wen and E. J. Cairns, *J. Electrochem. Soc.*, 1996, **143**, 1821–1827.
48 P. Birke, W. F. Chu and W. Weppner, *Solid State Ionics*, 1996, **93**, 1–15.
49 H. Sato, D. Takahashi, T. Nishina and I. Uchida, *J. Power Sources*, 1997, **68**, 540–544.
50 J. M. McGraw, C. S. Bahn, P. A. Parilla, J. D. Perkins, D. W. Readey and D. S. Ginley, *Electrochim. Acta*, 1999, **45**, 187–196.
51 Y.-I. Jang, B. J. Neudecker and N. J. Dudney, *Electrochem. Solid-State Lett.*, 2001, **4**, A74.

52 Y. Iriyama, M. Inaba, T. Abe and Z. Ogumi, *J. Power Sources*, 2001, **94**, 175–182.

53 P. J. Bouwman, B. A. Boukamp, H. J. M. Bouwmeester and P. H. L. Notten, *J. Electrochem. Soc.*, 2002, **149**, A699–A709.

54 H. Xia, L. Lu and G. Ceder, *J. Power Sources*, 2006, **159**, 1422–1427.

55 J. Xie, N. Imanishi, A. Hirano, M. Matsumura, Y. Takeda and O. Yamamoto, *Solid State Ionics*, 2007, **178**, 1218–1224.

56 S. B. Tang, M. O. Lai and L. Lu, *J. Alloys Compd.*, 2008, **449**, 300–303.

57 S. Shiraki, H. Oki and T. Hitosugi, *Surf. Interface Anal.*, 2016, **48**, 1240–1243.

58 Y.-H. Wen, E.-B. Yang, S.-J. Xiang, L.-A. Fu and S.-Q. Fang, *J. Radioanal. Nucl. Chem.*, 2001, **247**, 199–203.

59 J. Crank, *The mathematics of diffusion*, Oxford University Press, 1979.

60 W. Weppner and R. A. Huggins, *J. Electrochem. Soc.*, 1977, **124**, 1569–1578.

61 C. J. Wen, B. A. Boukamp, R. A. Huggins and W. Weppner, *J. Electrochem. Soc.*, 1979, **126**, 2258–2266.

62 G. Kresse and J. Furthmüller, *Phys. Rev. B: Condens. Matter Mater. Phys.*, 1996, **54**, 11169–11186.

63 J. P. Perdew, K. Burke and M. Ernzerhof, *Phys. Rev. Lett.*, 1996, **77**, 3865–3868.

64 P. E. Blöchl, *Phys. Rev. B: Condens. Matter Mater. Phys.*, 1994, **50**, 17953–17979.

65 D. Sheppard, R. Terrell and G. Henkelman, *J. Chem. Phys.*, 2008, **128**, 134106.

66 G. Henkelman, B. P. Uberuaga and H. Jónsson, *J. Chem. Phys.*, 2000, **113**, 9901–9904.

67 M. Antaya, K. Cearns, J. S. Preston, J. N. Reimers and J. R. Dahn, *J. Appl. Phys.*, 1994, **76**, 2799–2806.

68 J. Rahn, E. Huger, L. Dorrer, B. Ruprecht, P. Heitjans and H. Schmidt, *Phys. Chem. Chem. Phys.*, 2012, **14**, 2427–2433.

69 J. Rahn, P. Heitjans and H. Schmidt, *J. Phys. Chem. C*, 2015, **119**, 15557–15561.

70 S. Levasseur, M. Ménétrier, Y. Shao-Horn, L. Gautier, A. Audemer, G. Demazeau, A. Largeteau and C. Delmas, *Chem. Mater.*, 2003, **15**, 348–354.

71 S.-W. Kim and S.-I. Pyun, *Electrochim. Acta*, 2001, **46**, 987–997.

72 R. Kutner, *Phys. Lett. A*, 1981, **81**, 239–240.

73 T. Kudo, M. Hibino and I. Honma, Uchida Rokakuho, Science of lithium-ion battery, Tokyo, 2010, in Japanese.